



LAWRENCE
LIVERMORE
NATIONAL
LABORATORY

Least-Squares Wave-Front Reconstruction of Shack-Hartmann Sensors and Shearing Interferometers using Multigrid Techniques

K. L. Baker

February 10, 2005

Review of Scientific Instruments

Disclaimer

This document was prepared as an account of work sponsored by an agency of the United States Government. Neither the United States Government nor the University of California nor any of their employees, makes any warranty, express or implied, or assumes any legal liability or responsibility for the accuracy, completeness, or usefulness of any information, apparatus, product, or process disclosed, or represents that its use would not infringe privately owned rights. Reference herein to any specific commercial product, process, or service by trade name, trademark, manufacturer, or otherwise, does not necessarily constitute or imply its endorsement, recommendation, or favoring by the United States Government or the University of California. The views and opinions of authors expressed herein do not necessarily state or reflect those of the United States Government or the University of California, and shall not be used for advertising or product endorsement purposes.

Least-Squares Wave-Front Reconstruction of Shack-Hartmann Sensors and Shearing Interferometers using Multigrid Techniques

K.L. Baker

Lawrence Livermore National Laboratory, Livermore, CA, USA

Abstract

This article details a multigrid algorithm that is suitable for least squares wave-front reconstruction of Shack-Hartmann and shearing interferometer wave-front sensors. The algorithm detailed in this article is shown to scale with the number of sub-apertures in the same fashion as fast Fourier transform techniques, making it suitable for use in applications requiring a large number of sub-apertures and high Strehl ratio systems such as for high spatial frequency characterization of high density plasmas, optics metrology and multi-conjugate and extreme adaptive optics systems.

PACS: 52.70.Kz, 52.70.-m

I. Introduction

Electron density measurements in high-density plasmas have been obtained using a variety of techniques, including interferometry,¹ moiré deflectometry,² grid image refractometry³ and plasma emission spectroscopy.⁴ Each of these techniques have limitations associated with their use. Both interferometry and moiré deflectometry measurements suffer from ambiguity when the density gradients become large enough such that the interferogram undergoes indiscernible jumps between fringes. In addition, moiré deflectometry measures the gradient of the density profile transverse to the fringe pattern and, therefore, requires two orthogonal measurements to determine the two-dimensional density profile. Plasma emission spectroscopy requires accurate knowledge of both the temperature and density profiles along the chordal measurement through the plasma and sophisticated atomic physics codes, as well as carefully calibrated instruments.

Recently, the use of Shack-Hartmann wave-front sensors to measure the phase of an aberrated beam passing through a plasma has been proposed.^{5,6} Shack-Hartmann wave-front sensors have primarily been used to measure the wave-front of light after propagation through the atmosphere,^{7,8} for optical metrology⁹ and to look at the propagation characteristics of lasers¹⁰. Shack-Hartmann wave-front sensors measure the local wave-front tilt perpendicular to the probe laser. As such, it provides 2-D orthogonal information unlike moiré deflectometry, which only measures parameters in the direction transverse to the fringe pattern. All of the light that passes through the plasma can be collected by the lenslet array giving it a higher optical efficiency than either moiré deflectometry, which utilizes two Ronchi rulings to produce an interference pattern, or

interferometry, which utilizes beamsplitters to form and recombine the different paths of the interferometer. Shack-Hartmann sensors can easily operate with broadband or low coherence light, where interferometric measurements are more difficult. In addition, a density measurement based on a Shack-Hartmann sensor requires fewer optical components than are required in moiré deflectometry and interferometry and the aberrations present in the optical system can be accounted for, allowing less expensive optics to be used.

This article examines the problem of least-squares wave-front reconstruction given a measurement of the phase gradient such as obtained from Shack-Hartmann and shear interferometer wave-front sensors. In particular, an algorithm based on multigrid techniques is developed to solve the partial differential equations that result from least-squares wave-front reconstruction from measurements obtained using Shack-Hartmann wave-front sensors and shearing interferometers. The multigrid technique is reviewed in the next section. The third section shows results using the algorithms and provides a summary of the work presented. The equations representing the least-squares wave-front reconstruction are derived in the appendix.

II. Review of Multigrid Techniques

Iterative techniques such as Gauss elimination, Gauss-Seidel relaxation and simultaneous over-relaxation are very efficient at quickly solving for high spatial frequencies, however, they are quite slow in obtaining low spatial frequencies and require many iterations to do so. The multigrid approach solves a particular problem on multiple grids, each with a different scale, transferring the residual error between the grids. This

allows low spatial frequencies on the finest grid to be transformed into high spatial frequencies on the coarsest grid where they can be solved quickly using the above mentioned techniques such as Gauss-Seidel relaxation. These “high spatial frequencies” on the coarsest grid are then transformed back into low spatial frequencies on the finest grid. This allows multigrid techniques to solve problems very quickly for both the low and high spatial frequencies. The algorithm detailed below was implemented in the Interactive Data Language (IDL) programming language and as shown below solves the least-squares phase reconstruction problem on an $N \times N$ grid in $O(N^2 \log N)$, which follows the same scaling as fast Fourier transform techniques.^{11,12,13,14} The multigrid techniques, however, can solve any size grid without incurring a speed penalty for non-power of 2 grids such as occurs with Fourier transform techniques. Multigrid techniques have been implemented as $O(N)$ solvers, making them the optimal technique.¹⁵ In addition, multigrid algorithms can be parallelized easily and efficiently.

In the multigrid technique, the “residual error” of the equations is transferred to the coarser grid via a restriction operator described below. For the linear problem $A\Phi = \rho$, the residual equation is defined as $Ae = \rho - A\phi$, where ϕ is an approximation to Φ and e is the unknown error $\Phi - \phi$. Relaxation on $A\Phi = \rho$, with initial guess of ϕ is equivalent to relaxing on $Ae = r$ with initial guess $e = 0$, where r is residual error $r = \rho - A\phi$.^{16,17}

The process of transferring from the fine grid to the coarse grid is accomplished with a restriction operator. The concept of restriction in one dimension is shown in Fig. 1. The fine grid is transferred to the coarse grid with the restriction operator and sampled at every other point, resulting in a factor of two reduction in the grid dimensions. In this case the values at points on the coarse grid are made up of half of the value on the

corresponding fine grid plus one quarter of the values on either side. In two dimensions, the restriction operator takes the form^{16,17}

$$c_{i,j} = (f_{2i-1,2j-1} + f_{2i+1,2j-1} + f_{2i-1,2j+1} + f_{2i+1,2j+1})/16 \\ (f_{2i,2j-1} + f_{2i,2j+1} + f_{2i-1,2j} + f_{2i+1,2j})/8 + f_{2i,2j} / 4, \quad (1)$$

where the variable f denotes points on the fine grid and the variable c denotes points on the coarse grid.

The process of transferring from the coarse grid to the fine grid is accomplished with a prolongation operator. The concept of prolongation or interpolation in one dimension is shown in Fig. 2. Prolongation allows for a transfer of the solution from the coarse grid to the fine grid. In this case the values at points on the coarse grid map, corresponding to points on the fine grid, remain unchanged as they are mapped to the fine grid. The values at fine-grid points that do not correspond to the coarse grid nodes are the averages of their coarse-grid neighbors. In two dimensions, the prolongation process is simply bilinear interpolation^{16,17}

$$f_{2i,2j} = c_{i,j} \\ f_{2i+1,2j} = 0.5(c_{i,j} + c_{i+1,j}) \\ f_{2i,2j+1} = 0.5(c_{i,j} + c_{i,j+1}) \\ f_{2i+1,2j+1} = 0.25(c_{i,j} + c_{i+1,j} + c_{i,j+1} + c_{i+1,j+1}), \quad (2)$$

where again the variable f denotes points on the fine grid and the variable c denotes points on the coarse grid.

The basic algorithm for the multigrid technique is known as the V-cycle.^{16,17} The V-cycle relaxes the original equation on the finest grid and then restricts the residual to the grid that is a factor of two smaller. This process continues until the coarsest grid is reached at which time the equation goes through the prolongation operation until the

finest grid is reached again. The V-cycle process is shown pictorially in Fig. 3 and the flowchart¹⁷ of the algorithm is displayed in Fig. 4 for going from the finest grid to the coarsest grid and back.

The full multigrid cycle uses the V-cycle described above to obtain better results than using the V-cycle alone. The full multigrid cycle is shown pictorially in Fig. 5 and the flowchart¹⁷ for the algorithm is given in Fig. 6. In the full multigrid cycle, the original equation is relaxed on the finest grid and the residual is restricted to the grid a factor of two smaller. This process is continued until the coarsest grid is reached. The prolongation operator is then used to bring the process to the grid, which is a factor of two finer than the coarsest grid. The V-cycle process is then called iteratively, each time the bringing the process back to a grid, which is a factor of two finer than the starting grid until the finest grid is reached.

The boundary conditions for the phase reconstruction problem are derived via a mirror reflection of the phase, Φ , as depicted in Fig. 7.¹⁴ The phase is defined on the interval $0 \leq i \leq p-1$ and $0 \leq j \leq q-1$. The phase is reflected about the line $i=p-1$ and about $j=q-1$, which creates a periodic function in which the boundary conditions for the phase derivative are readily derived. The phase function for the lower left-hand corner is shown in Fig. 8, which allows for easy identification of the following boundary conditions:¹⁴

$$\begin{aligned}
 \frac{\partial \Phi}{\partial x}_{-1,j} &= -\frac{\partial \Phi}{\partial x}_{0,j} \\
 \frac{\partial \Phi}{\partial x}_{p-1,j} &= -\frac{\partial \Phi}{\partial x}_{p-2,j} \\
 \frac{\partial \Phi}{\partial y}_{i,-1} &= -\frac{\partial \Phi}{\partial y}_{i,0} \\
 \frac{\partial \Phi}{\partial y}_{i,q-1} &= -\frac{\partial \Phi}{\partial y}_{i,q-2}
 \end{aligned} \tag{3}$$

The phase is still solved on the original grid $0 \leq i \leq p-1$ and $0 \leq j \leq q-1$. The mirror reflection is simply used to provide the appropriate boundary conditions, which must be imposed after each restriction operation to ensure that the correct solution is reached.

III. Reconstruction Results

The wave-front reconstruction algorithm described in the previous section was implemented on the equations derived in the appendix for the case of the shearing interferometer, Eq. A5 in the Hudgin geometry, and for the Shack-Hartmann sensor, Eq. A9 in the Fried geometry. The phase profile was chosen to resemble a plasma produced by a high intensity laser interaction with a solid target. The phase profile was therefore primarily a linear phase ramp¹⁸ with a Kolmogorov turbulence profile,¹⁹ as shown in Fig. 8. The phase gradients are obtained by taking the appropriate derivatives of the phase profile for both the Hudgin and Fried geometries. The Hudgin phase gradients are defined as $\phi_{xi,j} = \Phi_{i,j} - \Phi_{i-1,j}$ for the x slope and $\phi_{yi,j} = \Phi_{i,j} - \Phi_{i,j-1}$ for the y slope, where $\phi_{xi,j}$ and $\phi_{yi,j}$ represent partial derivatives of the phases in the x and y directions, respectively. The Fried phase gradients are defined as $\phi_{xi,j} = (\Phi_{i+1/2,j+1/2} + \Phi_{i+1/2,j-1/2} - \Phi_{i-1/2,j+1/2} - \Phi_{i-1/2,j-1/2})$ and $\phi_{yi,j} = (\Phi_{i+1/2,j+1/2} + \Phi_{i-1/2,j+1/2} - \Phi_{i+1/2,j-1/2} - \Phi_{i-1/2,j-1/2})$, where $\phi_{xi,j}$ and $\phi_{yi,j}$ represent partial derivatives of the phases in the center of the sub-aperture in the x and y directions, respectively.

The initial phase primarily consists of a linear phase ramp with approximately 10 waves peak to valley. The appropriate gradients, as detailed above, were taken and then the original phase was reconstructed using the multigrid algorithm detailed in this article. The reconstruction results are shown in Fig. 9. In this case the initial phase is shown in

Fig. 9a, along with the difference between the reconstructed phase and the initial phase for the Hudgin geometry, Fig. 9 b, and the Fried geometry, Fig. 9 c. The reconstructed phases shown in Fig 9b and 9c resulted from two cycles of the multigrid algorithm. The variance as a function of full multigrid cycles for the two separate geometries is then shown in Fig. 10. The variance is defined as the average value of the square of the difference between the reconstructed phase and the original phase. The variance for the Hudgin geometry is shown in Fig. 10 as the solid black line and the variance for the Fried geometry is shown in Fig. 10 as the solid gray line. This figure shows that the multigrid algorithm very quickly converges to the correct solution. By the second full multigrid cycle, the Hudgin geometry produced a variance of less than 0.001 rad^2 and the Fried geometry had a variance of less than 0.013 rad^2 .

The algorithm solves the least-squares phase reconstruction problem on an $N \times N$ grid in $O(N^2 \log N)$, which follows the same scaling law as Fourier transform techniques. The scaling with the number of sub-apertures along a given side, N , ranging from 16 to 512 is shown in Fig. 11. In Fig. 11, the circles represent the actual run time for a given number of sub-apertures along a side and the black line represents the least-squares fit of an $N^2 \log N$ function. The multigrid algorithm, however, can solve any size grid without incurring a speed penalty for non-power of 2 grids such as occurs with Fourier transform techniques. This algorithm can also be readily adapted to a weighted scheme where sub-apertures with poor signal to noise ratio can be masked out during reconstruction to improve the results. This can occur with coherent sources, partially illuminated sub-apertures and also for atmospheric propagation when scintillation effects can become dominant.

The multigrid algorithm presented above is applicable to phase gradient detecting wave-front sensors, which include shearing interferometers, moiré deflectometry and Shack-Hartmann sensors. The particular multigrid algorithm presented in this article was shown above to have the same scaling with sub-apertures as previous Fourier transform techniques and the technique was demonstrated to converge quickly. Two full multigrid cycles resulted in a residual variance of less than 0.001 rad^2 for the Hudgin geometry and less than 0.013 rad^2 for the Fried geometry from an initial phase profile of greater than 60 radians peak to valley. This favorable scaling with actuator number makes this technique attractive for applications requiring a large number of sub-apertures such as high spatial frequency characterization of high density plasmas, optics metrology and multi-conjugate and extreme adaptive optics systems.

Acknowledgement

This work was performed under the auspices of the U.S. Department of Energy by the University of California, Lawrence Livermore National Laboratory under contract No. W-7405-Eng-48.

Appendix A Review of the Equations Governing Least-Squares Phase Reconstruction

In both shearing interferometers and Shack-Hartmann sensors the slopes of the wave-front are detected across the aperture of the system. From these phase slope measurements, the wave-front incident upon the aperture can be reconstructed. One technique for reconstruction is the method of least-squares wave-front reconstruction. The object of this technique is to minimize the difference between the derivative of the reconstructed phase and the measured phase derivative at each of the points in the aperture in the least-squares sense. That implies the minimization of the equation²⁰

$$\varepsilon^2 = \sum_{i,j} \left(\frac{\partial \Phi}{\partial x}_{i,j} - \frac{\partial \psi}{\partial x}_{i,j} \right)^2 + \left(\frac{\partial \Phi}{\partial y}_{i,j} - \frac{\partial \psi}{\partial y}_{i,j} \right)^2, \quad (\text{A1})$$

where Φ represents the reconstructed phase and $\partial\psi/\partial x$ and $\partial\psi/\partial y$ represents the measured x and y phase derivatives, respectively. The minimization of Eq. A1 is dependent upon the geometry from which the phase derivatives are measured as detailed below.

The two most common geometries used in phase reconstruction, the Hudgin²¹ and Fried²⁰ geometries, are shown in Figure A1. The Hudgin geometry, shown in Figure A.1, is most commonly used for shearing interferometers or for moiré deflectometry, but has also been applied to Shack-Hartmann wave-front sensors. This geometry measures both the phase and the phase derivatives using the same grid. The derivative of the phase is a simple finite difference approximation expressed as $\phi_{xi,j} = \Phi_{i,j} - \Phi_{i-1,j}$ for the x slope and $\phi_{yi,j} = \Phi_{i,j} - \Phi_{i,j-1}$ for the y slope, where $\phi_{xi,j}$ and $\phi_{yi,j}$ represent partial derivatives of the phases in the x and y directions, respectively. The minimization of Eq. A1 is achieved by

taking a derivative of the residual error, ϵ^2 , with respect to the reconstructed phase and setting it to zero. The phases in the separate sub-apertures are assumed to be independent from one another. When these phase derivatives are placed in Eq. A1 above, the minimization of Eq. A1 takes the form

$$\frac{\partial \epsilon^2}{\partial \Phi_{p,q}} = 0 = 2 \sum_{i,j} \left(\frac{\partial \Phi}{\partial x_{i,j}} - \frac{\partial \psi}{\partial x_{i,j}} \right) \left(\frac{\partial \Phi_{i+1,j}}{\partial \Phi_{p,q}} - \frac{\partial \Phi_{i,j}}{\partial \Phi_{p,q}} \right) + \left(\frac{\partial \Phi}{\partial y_{i,j}} - \frac{\partial \psi}{\partial y_{i,j}} \right) \left(\frac{\partial \Phi_{i,j+1}}{\partial \Phi_{p,q}} - \frac{\partial \Phi_{i,j}}{\partial \Phi_{p,q}} \right) \quad (A2)$$

Because of the assumption of independence, there is only a contribution from the derivatives when the two phases are from the same sub-aperture. This can be expressed in terms of delta functions, allowing Eq. A2 to be rewritten as

$$\frac{\partial \epsilon^2}{\partial \Phi_{p,q}} = 0 = 2 \sum_{i,j} \left(\frac{\partial \Phi}{\partial x_{i,j}} - \frac{\partial \psi}{\partial x_{i,j}} \right) \left(\delta_{p,i+1} \delta_{q,j} - \delta_{p,i} \delta_{q,j} \right) + \left(\frac{\partial \Phi}{\partial y_{i,j}} - \frac{\partial \psi}{\partial y_{i,j}} \right) \left(\delta_{p,i} \delta_{q,j+1} - \delta_{p,i} \delta_{q,j} \right) \quad (A3)$$

By multiplying the delta functions through the equation after replacing the phase derivatives with their finite difference approximation, the following equation is arrived at for phase reconstruction in the Hudgin geometry

$$\frac{\partial \epsilon^2}{\partial \Phi_{p,q}} = 0 = 2 \sum_{p,q} \left(\nabla^2 \Phi_{p,q} - \nabla \cdot \left(\nabla \psi_{p,q} \right) \right) \quad (A4)$$

This simply represents the Poisson equation, $\nabla^2\Phi = \rho$, with ρ equal to the divergence of the measured phase derivatives. The equivalent Gauss-Seidel iteration, used as the relaxation method in the multigrid algorithm for the Hudgin geometry, is

$$4\Phi_{p,q} = \Phi_{p+1,q-1} + \Phi_{p+1,q+1} + \Phi_{p-1,q+1} + \Phi_{p-1,q-1} - \psi_{x,p,q} + \psi_{x,p-1,q} - \psi_{y,p,q} + \psi_{y,p,q-1}, \quad (\text{A5})$$

where ψ_x and ψ_y represent the measured x and y phase derivative measurements, respectively.

The Fried geometry²⁰, also shown in Figure A1, is commonly used for Shack-Hartmann wave-front sensors. This geometry measures the phase and the phase derivatives on grids that are displaced relative to one another as shown in Figure A1. The derivative of the phase, Φ , in the center of a sub-aperture is dependent on the phase at the four corners of the sub-aperture. A finite difference approximation to the derivative can be expressed as $\phi_{xi,j} = (\Phi_{i+1/2,j+1/2} + \Phi_{i+1/2,j-1/2} - \Phi_{i-1/2,j+1/2} - \Phi_{i-1/2,j-1/2})$ and $\phi_{yi,j} = (\Phi_{i+1/2,j+1/2} + \Phi_{i-1/2,j+1/2} - \Phi_{i+1/2,j-1/2} - \Phi_{i-1/2,j-1/2})$, where $\phi_{xi,j}$ and $\phi_{yi,j}$ represent derivatives of the phases in the center of the sub-aperture in the x and y directions, respectively. The minimization of Eq. A1 is again achieved by taking a derivative of the residual error, ϵ^2 , with respect to the reconstructed phase after the phase derivative expressions for the Fried geometry have been inserted into Eq. A1. The minimization then takes the form

$$\begin{aligned}
\frac{\partial^2 \epsilon}{\partial \Phi_{p,q}} = 0 &= 2 \sum_{i,j} \left(\frac{\partial \Phi}{\partial x_{i,j}} - \frac{\partial \psi}{\partial x_{i,j}} \right)^* \\
&+ \left(\frac{\partial \Phi}{\partial y_{i,j}} - \frac{\partial \psi}{\partial y_{i,j}} \right)^* \\
&\frac{1}{2} \left(\frac{\partial \Phi_{i+1/2, j+1/2}}{\partial \Phi_{p,q}} + \frac{\partial \Phi_{i+1/2, j-1/2}}{\partial \Phi_{p,q}} - \frac{\partial \Phi_{i-1/2, j+1/2}}{\partial \Phi_{p,q}} - \frac{\partial \Phi_{i-1/2, j-1/2}}{\partial \Phi_{p,q}} \right) \quad (A6) \\
&\frac{1}{2} \left(\frac{\partial \Phi_{i+1/2, j+1/2}}{\partial \Phi_{p,q}} + \frac{\partial \Phi_{i-1/2, j+1/2}}{\partial \Phi_{p,q}} - \frac{\partial \Phi_{i+1/2, j-1/2}}{\partial \Phi_{p,q}} - \frac{\partial \Phi_{i-1/2, j-1/2}}{\partial \Phi_{p,q}} \right)
\end{aligned}$$

Again because of the assumption of independence of the different sub-aperture phases, there is only a contribution from the derivatives when the two phases correspond to the same location. This can be expressed in terms of delta functions, allowing Eq. A6 to be written as

$$\begin{aligned}
0 &= \sum_{i,j} \left(\Phi_{i+1/2, j+1/2} + \Phi_{i+1/2, j-1/2} - \Phi_{i-1/2, j+1/2} - \Phi_{i-1/2, j-1/2} \right. \\
&\quad \left. + \psi_{x_{i+1/2, j+1/2}} + \psi_{x_{i+1/2, j-1/2}} - \psi_{x_{i-1/2, j+1/2}} + \psi_{x_{i-1/2, j-1/2}} \right)^* \\
&\quad \left(d_{p,i+1/2} d_{q,j+1/2} + d_{p,i+1/2} d_{q,j-1/2} - d_{p,i-1/2} d_{q,j+1/2} - d_{p,i-1/2} d_{q,j-1/2} \right) \quad (A7) \\
&\quad + \left(\Phi_{i+1/2, j+1/2} + \Phi_{i-1/2, j+1/2} - \Phi_{i+1/2, j-1/2} - \Phi_{i-1/2, j-1/2} \right. \\
&\quad \left. + \psi_{x_{i+1/2, j+1/2}} + \psi_{x_{i-1/2, j+1/2}} - \psi_{x_{i+1/2, j-1/2}} + \psi_{x_{i-1/2, j-1/2}} \right)^* \\
&\quad \left(d_{p,i+1/2} d_{q,j+1/2} + d_{p,i-1/2} d_{q,j+1/2} - d_{p,i+1/2} d_{q,j-1/2} - d_{p,i-1/2} d_{q,j-1/2} \right)
\end{aligned}$$

where ψ_x and ψ_y represent the measured x and y phase derivative measurements, respectively. Multiplying the delta functions through Eq. A7, the following equation is

arrived at for phase reconstruction in the Fried geometry when both the phase being reconstructed and the measured phase derivatives are placed on a common grid

$$\frac{\partial^2 \epsilon}{\partial \Phi_{p,q}} = 0 = \sum_{p,q} \left(\begin{aligned} &4\nabla^2 \Phi_{p,q} + 2 \frac{\partial^4 \Phi_{p,q}}{\partial^2 x \partial^2 y} + \frac{\partial^2}{\partial^2 x} \left(4\psi_{xp,q} + \frac{\partial^2 \psi_{xp,q}}{\partial^2 y} \right) \\ &+ \frac{\partial^2}{\partial^2 y} \left(4\psi_{yp,q} + \frac{\partial^2 \psi_{yp,q}}{\partial^2 x} \right) \end{aligned} \right). \quad (\text{A8})$$

Least-squares wave-front reconstruction in the Fried geometry yields a slightly more complicated partial differential equation than the Poisson equation obtained in the Hudgin geometry. The Gauss-Seidel iteration used as the relaxation method in the multigrid algorithm for the Fried geometry, is²⁰

$$\begin{aligned} 4\Phi_{p,q} = & \Phi_{p+1,q-1} + \Phi_{p+1,q+1} + \Phi_{p-1,q+1} + \Phi_{p-1,q-1} + \\ & 0.5 \left[\begin{aligned} &\psi_x_{p+0.5,q+0.5} + \psi_x_{p+0.5,q-0.5} - \psi_x_{p-0.5,q+0.5} - \psi_x_{p-0.5,q-0.5} \end{aligned} \right] +, \quad (\text{A9}) \\ & 0.5 \left[\begin{aligned} &\psi_y_{p+0.5,q+0.5} + \psi_y_{p-0.5,q+0.5} - \psi_y_{p+0.5,q-0.5} - \psi_y_{p-0.5,q-0.5} \end{aligned} \right] \end{aligned}$$

where ψ_x and ψ_y represent the x and y phase derivative measurements on the displaced grid, respectively.

REFERENCES

with titles

- ¹ Garland E. Busch, "Holographic Interferometry," Rev. Sci. Instrum. **56**, 879 (1985).
- ² B. Moosman, V.M. Bystritskii, C.J. Boswell et al., "Moire deflectrometry diagnostic for transient plasma, using a multipulse N2 laser," Rev. Sci. Instrum. **67** (1), 170 (1996).
- ³ R. S. Craxton, F. S. Turner, R. Hoefen et al., "Characterization of laser-produced plasma density profiles using grid image refractometry," Phys. Fluids B **12**, 4419 (1993).
- ⁴ I. H. Hutchinson, *Principles of Plasma Diagnostics*. (Cambridge University Press, Cambridge, 1987).
- ⁵ K. L. Baker, J. Brase, M. Kartz et al., "The use of a Shack–Hartmann wave front sensor for electron density characterization of high density plasmas," REVIEW OF SCIENTIFIC INSTRUMENTS **73** (11), 3784 (2002).
- ⁶ K. L. Baker, J. Brase, M. Kartz et al., "Electron density characterization by use of a broadband x-ray-compatible wave-front sensor," OPTICS LETTERS **28** (3), 149 (2003).
- ⁷ John W. Hardy, *Adaptive Optics for Astronomical Telescopes*. (Oxford University Press, Oxford, 1998).
- ⁸ S. S. Olivier, J. An, K. Avicola et al., "Performance of laser guide star adaptive optics at Lick Observatory," SPIE **2534**, 26 (1995).

- ⁹ Jeffrey A. Koch, Robert W. Presta, Richard A. Sacks et al., "Experimental comparison of a Shack-Hartmann sensor and a phase-shifting interferometer for large-optics metrology applications," *Applied Optics* **39** (25), 4540 (2000).
- ¹⁰ Bernd Schafer and Klaus Mann, "Investigation of the propagation characteristics of excimer lasers using a Hartmann-Shack sensor," *Review of Scientific Instruments* **71** (7), 2663 (2000).
- ¹¹ Hiroaki Takajo and Tohru Takahashi, "Noniterative method for obtaining the exact solution for the normal equation in least-squares phase estimation from the phase difference," *J. Opt. Soc. Am. A* **5** (11), 1818 (1988).
- ¹² Hiroaki Takajo and Tohru Takahashi, "Least-squares phase estimation from the phase difference," *J. Opt. Soc. Am. A* **5** (3), 416 (1988).
- ¹³ Lisa A. Poyneer, Donald T. Gavel, and James M. Brase, "Fast wave-front reconstruction in large adaptive optics systems with use of the Fourier transform," *J. Opt. Soc. Am. A* **19** (10), 2100 (2002).
- ¹⁴ Mark D. Pritt and Jerome S. Shipman, "Least-squares Two-Dimensional Phase Unwrapping Using FFT's," *IEEE Transactions on Geoscience and Remote Sensing* **32** (3), 706 (1994).
- ¹⁵ L. Gilles, "Order-N sparse minimum-variance open-loop reconstructor for extreme adaptive optics," *Optics Letters* **28** (20), 1927 (2003).
- ¹⁶ W. L. Briggs, *A Multigrid Tutorial*. (SIAM, Philadelphia, 1987).
- ¹⁷ Mark D. Pritt, "Phase Unwrapping by Means of Multigrid Techniques for Interferometric SAR," *IEEE Transactions on Geoscience and Remote Sensing* **34** (3), 728 (1996).

- ¹⁸ William L. Kruer, *The Physics of Laser Plasma Interactions*. (Addison-Wesley Publishing Company, Inc., Redwood City, California, 1988).
- ¹⁹ A.N. Kolmogorov, in *Turbulence, Classic Papers on Statistical Theory*, edited by S.K. Friedlander and L. Topper (Interscience, New York, 1961).
- ²⁰ David L. Fried, "Least-square fitting a wave-front distortion estimate to an array of phase-difference measurements," *Journal of the Optical Society of America* **67** (3), 370 (1977).
- ²¹ Richard Hudgin, "Wave-front compensation error due to finite corrector-element size," *J. Opt. Soc. Am.* **67** (3), 393 (1977).

REFERENCES

without titles

- ¹ Garland E. Busch, Rev. Sci. Instrum. **56**, 879 (1985).
- ² B. Moosman, V.M. Bystritskii, C.J. Boswell et al., Rev. Sci. Instrum. **67** (1), 170 (1996).
- ³ R. S. Craxton, F. S. Turner, R. Hoefen et al., Phys. Fluids B **12**, 4419 (1993).
- ⁴ I. H. Hutchinson, *Principles of Plasma Diagnostics*. (Cambridge University Press, Cambridge, 1987).
- ⁵ K. L. Baker, J. Brase, M. Kartz et al., REVIEW OF SCIENTIFIC INSTRUMENTS **73** (11), 3784 (2002).
- ⁶ K. L. Baker, J. Brase, M. Kartz et al., OPTICS LETTERS **28** (3), 149 (2003).
- ⁷ John W. Hardy, *Adaptive Optics for Astronomical Telescopes*. (Oxford University Press, Oxford, 1998).
- ⁸ S. S. Olivier, J. An, K. Avicola et al., SPIE **2534**, 26 (1995).
- ⁹ Jeffrey A. Koch, Robert W. Presta, Richard A. Sacks et al., Applied Optics **39** (25), 4540 (2000).
- ¹⁰ Bernd Schafer and Klaus Mann, Review of Scientific Instruments **71** (7), 2663 (2000).
- ¹¹ Hiroaki Takajo and Tohru Takahashi, J. Opt. Soc. Am. A **5** (11), 1818 (1988).
- ¹² Hiroaki Takajo and Tohru Takahashi, J. Opt. Soc. Am. A **5** (3), 416 (1988).
- ¹³ Lisa A. Poyneer, Donald T. Gavel, and James M. Brase, J. Opt. Soc. Am. A **19** (10), 2100 (2002).
- ¹⁴ Mark D. Pritt and Jerome S. Shipman, IEEE Transactions on Geoscience and Remote Sensing **32** (3), 706 (1994).

- ¹⁵ L. Gilles, Optics Letters **28** (20), 1927 (2003).
- ¹⁶ W. L. Briggs, *A Multigrid Tutorial*. (SIAM, Philadelphia, 1987).
- ¹⁷ Mark D. Pritt, IEEE Transactions on Geoscience and Remote Sensing **34** (3), 728 (1996).
- ¹⁸ William L. Kruer, *The Physics of Laser Plasma Interactions*. (Addison-Wesley Publishing Company, Inc., Redwood City, California, 1988).
- ¹⁹ A.N. Kolmogorov, in *Turbulence, Classic Papers on Statistical Theory*, edited by S.K. Friedlander and L. Topper (Interscience, New York, 1961).
- ²⁰ David L. Fried, Journal of the Optical Society of America **67** (3), 370 (1977).
- ²¹ Richard Hudgin, J. Opt. Soc. Am. **67** (3), 393 (1977).

FIGURE CAPTIONS

Figure 1 Pictorial representation of the restriction operation in the multigrid technique.

Figure 2 Pictorial representation of the prolongation operation in the multigrid technique.

Figure 3 Graphical depiction of the multigrid V-cycle.

Figure 4 Flowchart of the multigrid V-cycle

Figure 5 Graphical depiction of the full multigrid cycle.

Figure 6 Flowchart of the full multigrid cycle

Figure 7 Depiction of the mirror reflections used to determine the boundary conditions for the multigrid technique.

Figure 8 Phase values at the boundaries resulting from the mirror reflections. The phase gradients at the boundary are then readily determined from the measured gradients just inside the boundary.

Figure 9 The original phase from which the derivatives were derived is shown in Fig. 9a. The residual phase, resulting from reconstruction of the phase derivatives and subtraction from the original phase, for the Hudgin and Fried geometries are shown in Fig. 9b and Fig. 9c, respectively.

Figure 10 Phase Variance as a function of full multigrid cycles for the Hudgin and Fried geometries. The variance for the Hudgin geometry is denoted by the solid black line and for the Fried geometry by the solid gray line.

Figure 11 Scaling of the multigrid algorithm as a function of sub-aperture number along a side.

Figure A1 Two of the more common geometries used in wave-front reconstruction. The Hudgin geometry is displayed on the left and the Fried geometry on the right.

FIGURES

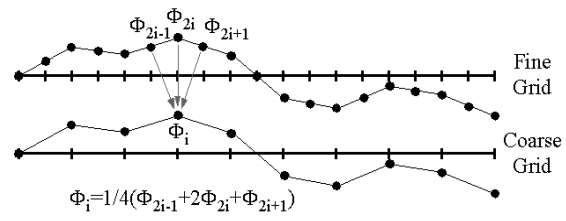


Figure 1

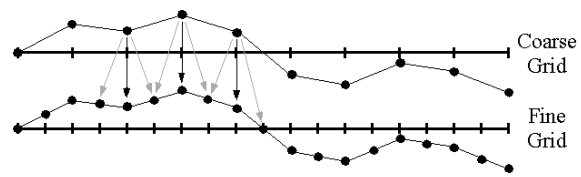


Figure 2

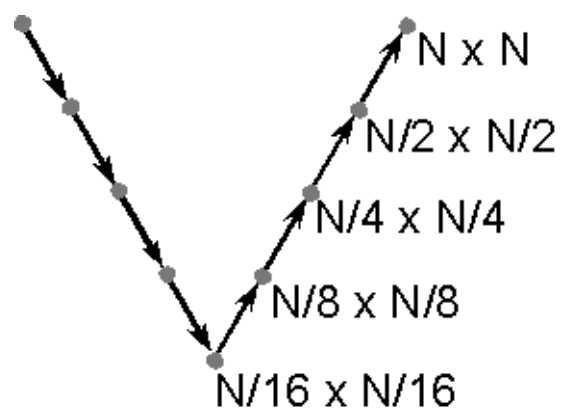


Figure 3

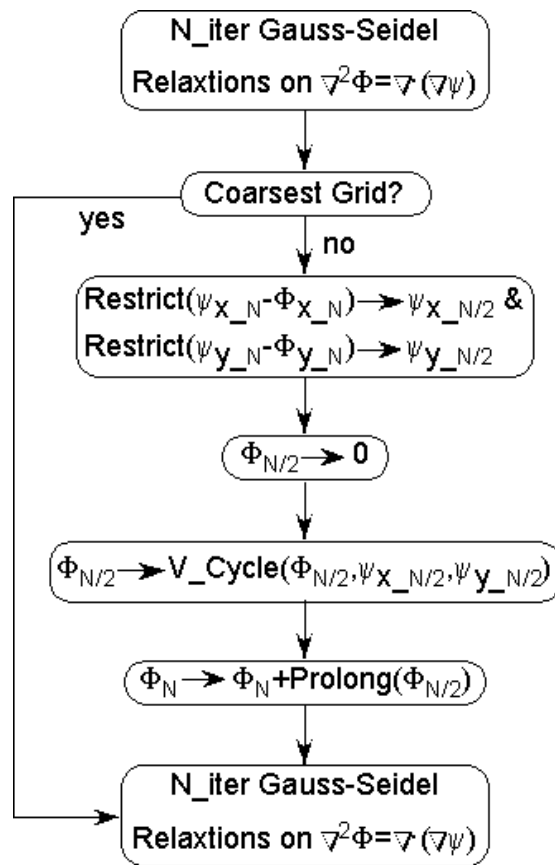


Figure 4

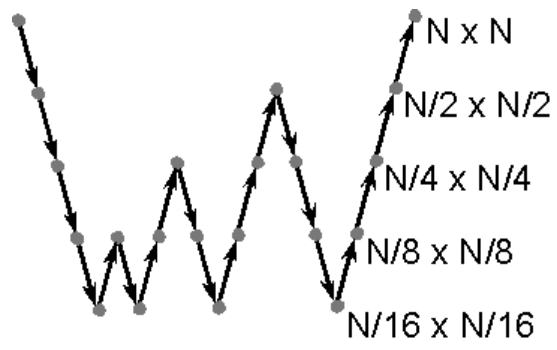


Figure 5

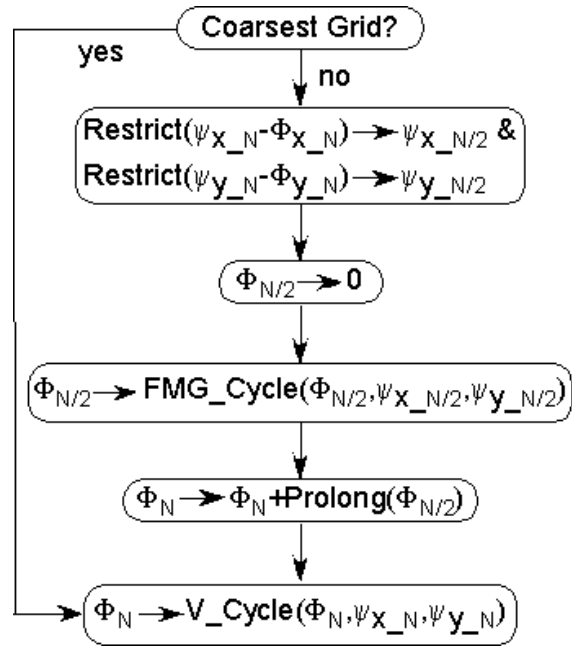


Figure 6

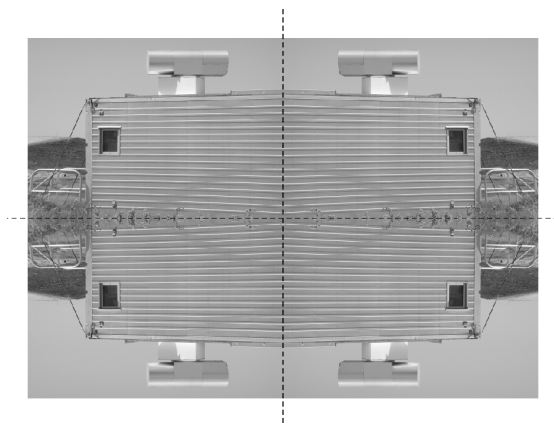


Figure 7

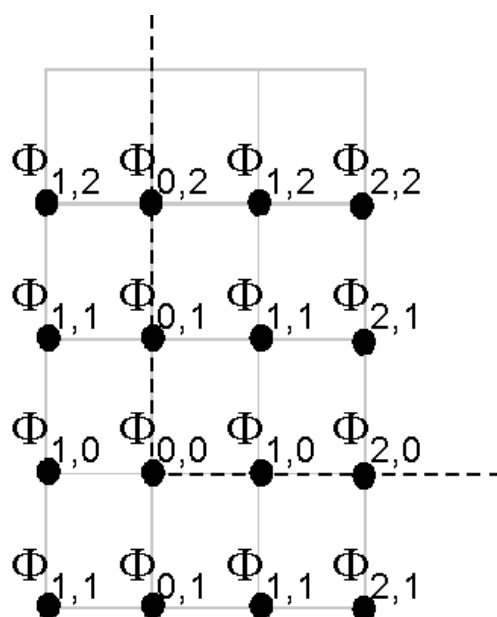


Figure 8

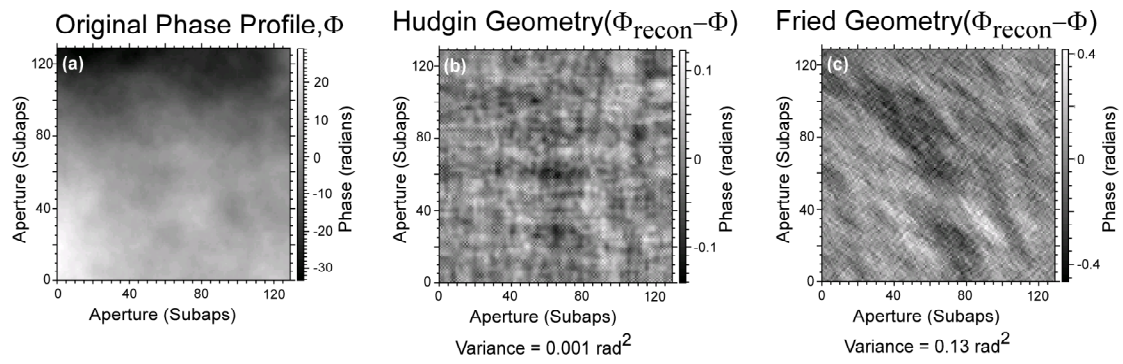


Figure 9

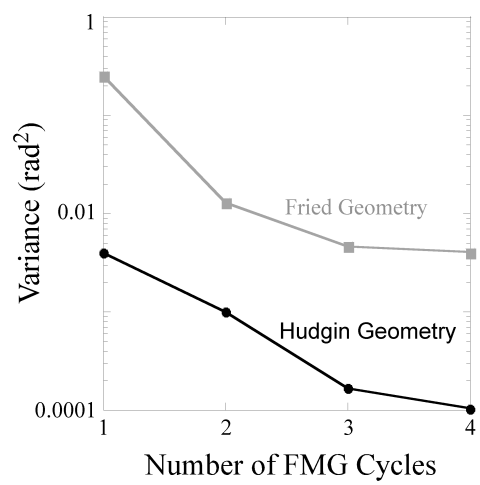


Figure 10

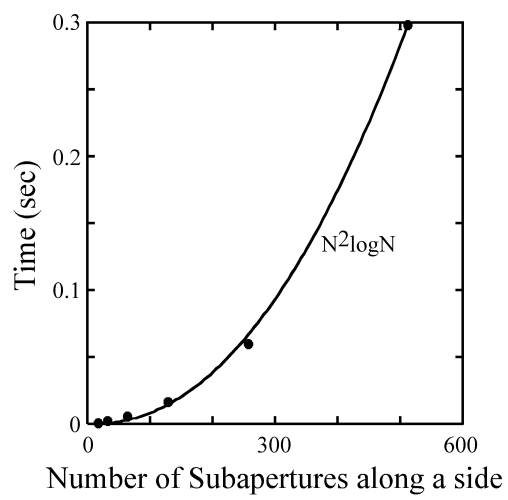


Figure 11

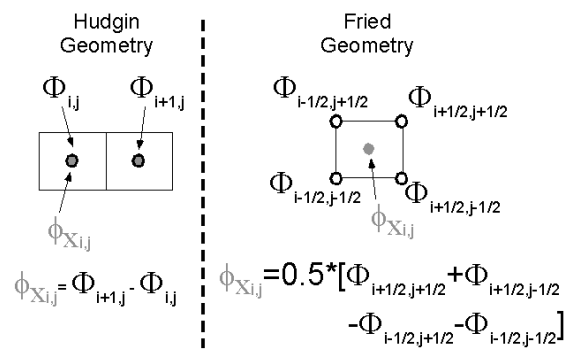


Figure A1